Structural Durability & Health Monitoring

Tech Science Press

Monitoring of Real-Time Complex Deformed Shapes of Thin-Walled Channel Beam Structures Subject to the Coupling Between Bi-Axial Bending and Warping Torsion

Rui Lu[1], Zhanjun Wu[1], Qi Zhou[1] and Hao Xu[1,*]

[1]School of Aeronautics and Astronautics, Faculty of Vehicle Engineering and Mechanics, State Key Laboratory of Structural Analysis for Industrial Equipment, Dalian University of Technology, Dalian, 116024, China.

[*]Corresponding Author: Hao Xu. Email: xuhao@dlut.edu.cn.

Abstract: Structural health monitoring (SHM) is a research focus involving a large category of techniques performing *in-situ* identification of structural damage, stress, external loads, vibration signatures, etc. Among various SHM techniques, those able to monitoring structural deformed shapes are considered as an important category. A novel method of deformed shape reconstruction for thin-walled beam structures was recently proposed by Xu et al. [1], which is capable of decoupling complex beam deformations subject to the combination of different loading cases, including tension/compression, bending and warping torsion, and also able to reconstruct the full-field displacement distributions. However, this method was demonstrated only under a relatively simple loading coupling cases, involving uni-axial bending and warping torsion. The effectiveness of the method under more complex loading cases needs to be thoroughly investigated. In this study, more complex deformations under the coupling between bi-axial bending and warping torsion was decoupled using the method. The set of equations for deformation decoupling was established, and the reconstruction algorithm for bending and torsion deformation were utilized. The effectiveness and accuracy of the method was examined using a thin-walled channel beam, relying on analysis results of finite element analysis (FEA). In the analysis, the influence of the positions of the measurement of surface strain distributions on the reconstruction accuracy was discussed. Moreover, different levels of measurement noise were added to the axial strain values based on numerical method, and the noise resistance ability of the deformation reconstruction method was investigated systematically. According to the FEA results, the effectiveness and precision of the method in complex deformation decoupling and reconstruction were demonstrated. Moreover, the immunity of the method to measurement noise was proven to be considerably strong.

Keywords: Structural health monitoring; deformation reconstruction; finite element analysis; strain measurement; channel section beam

1 Introduction

Structural health monitoring (SHM) is generally regarded as a large variety of techniques able of performing *in-situ* identification of structural damage, stress, external loads, vibration signatures, etc. In recent decades, intensive research interests have been focused on *in-situ* damage detection methods, most of which were established based on guided wave [2-5] and vibration theories [6-10]. Although structural damage, the presence, location and extent of which are considered as three main aspects to be evaluated, is with no doubt an important indicator directly associated with the integrity and safety of structures of interest, structural states (in terms of mechanical quantities such as strain/stress distribution, deformed shapes, external loads), on the other hand, are also important information needing increasing attentions, since these mechanical quantities are directly linked with structural operational states, which are vital for

the evaluation of structural performance and health situation, remaining service life prediction and even design optimization.

Among different state monitoring techniques, on-line monitoring of structural deformed shapes is of paramount significance, capable of giving real-time full-field distributions of displacement, strain and stress, as well as valuable feedbacks for active control. Specifically, the value of real time deformed shape sensing has been widely proven in fields including lightweight aircraft [11,12], satellites [13,14], robotics [15], medical apparatus [16], etc. In application of aerospace engineering, structural deformed shapes are usually captured using quantities such as static/dynamic displacements or strains. Displacement signals are considered to be directly related with deformed shapes. However, the acquisition of large sets of data of structural displacement in a real-time manner involves complex measurement devices (for example high-precision cameras), and thus difficult to be practically applied in aerospace application. On-board sensor networks measuring surface strain distributions, on the other hand, are more convenient to be installed. Thus the method of shape construction based on surface strains are considered promising and attract much research interests in recent years. The essential principle of deformed shape reconstruction by using strains resides on the establishment of reliable transfer function between the displacement field and the distribution of surface strains. When tackling structures with simple geometrics, for example, ideal beam, plate or shell structures, the classic geometric relationship linking displacement and surface strain can be well utilized and give precise reconstruction results. When facing structures with more complex geometries, the transfer function, as well as sensor layout, should be established more sophisticatedly, usually involving discrete representation of structural properties as adopted by finite element method. Typically, identified structural deformed shapes can be equivalently regarded as three-dimensional displacement fields of structures. Relying of the displacement fields, strain fields can be directly derived using the continuous or discrete geometric relations, and stress filed could be further calculated corresponding to the constitutive relations.

To date, a considerable amount of investigations relating to structural deformed shape reconstruction has been developed. An effective and efficient real-time deformed shape prediction method was developed based on Ko's theory [17-19], where beam-like structures are the main objects under investigation. In Ko's theory, surface strains were measured along the beam axis, and the continuous strain distributions were then approximated by using piecewise polynomials. The displacements were reconstructed using the strain distribution according to established displacement transfer functions. Although Ko's theory has been effectively applied in beam structures under bending case, large difficulty is associated with the task of reconstructing complex deformed shapes under complex loading cases. There are indeed satisfactory reconstruction results for the deformation case under the coupling between bending and torsion by using Ko's theory. However, the torsion deformations were actually derived indirectly, by using bending deformation data. Such a reconstruction accuracy may be high when treating beam structures having sections with large width-to-height ratios, in other words, those beams structures alike with plates. Under small width-to-height ratios, challenges in torsion deformation reconstruction will become severe. And classic beam torsion theory should be taken into account. Modal transformation algorithms were applied in another category of shape reconstruction methods, defined as modal methods [20,21]. In these methods, the strains measured on structural surface were linked with structural displacements through the transformation relationship between strain and displacement mode shapes. The effectiveness of modal methods has also been demonstrated in recent studies. However, some apparent obstacles hamper the application of the method in aerospace engineering. For example, the effectiveness of the model methods is highly sensitive to the accuracy of physical modeling, which means small degrees of uncertainty associated of factors such as material properties will cause large fluctuation of the shape reconstruction results. Another category of shape reconstruction method is established partially associated with traditional finite element method, defined as inverse finite element method (iFEM) [22-26]. The iFEM utilize the discrete relation between displacement and strain fields. Instead of the solution of the strain energy functional consists of strain and stress fields, the iFEM establish functional using theoretical and measured surface strain values, and estimate the displacement field inversely based on a

weighted least-squares variational principle. Using iFEM, deformed shapes of structures with complex geometries can be accurately constructed. However, a possible challenge of iFEM is that sophisticated sensor layout is often required to be consistent with FEM meshes. Moreover, compared with methods established on simple theoretical model, for example Ko's theory, iFEM is more time consuming when relatively large amount of computation for matrix solution is involved, which may cause certain time delay in real time monitoring.

Recently, a novel method of complex deformed shape reconstruction for thin-walled beam structures was proposed. The method is capable of decoupling complex deformations of thin-walled beam structures subject to the combination of different loading cases, including tension/compression, bi-axial bending and warping torsion. After deformation coupling, full-field displacement distribution can be constructed precisely using the decoupled deformation subject to individual loading cases. However, this method was demonstrated only under a relatively simple load coupling case, i.e., the coupling between uni-axial bending and warping torsion. The effectiveness of the method under more complex loading cases needs to be thoroughly investigated. In this study, more complex deformations under the coupling between bi-axial bending and warping torsion was decoupled. The set of equations for deformation decoupling was established, and the reconstruction algorithm for bending and torsion deformation were utilized. The effectiveness and accuracy of the method was examined using a thin-walled channel beam, relying on analysis results of finite element analysis (FEA). In the analysis, the influence of the positions of the measurement of surface strain distributions on the reconstruction accuracy was discussed. Moreover, different levels of measurement noise were added to the axial strain values based on numerical method, and the noise resistance ability of the deformation reconstruction method was investigated systematically. According to the FEA results, the effectiveness and precision of the method in complex deformation decoupling and reconstruction as was demonstrated. Moreover, the immunity of the method to measurement noise was proven to be considerably strong.

2 Theory

2.1 Deformation Decoupling for Thin-Walled Beam Structure Under Complex Loading Cases

As introduced in [27,28], the axial strain on the surface of a thin-walled beam structures can be interpreted to be associated with the contributions from combined loading cases including axial tension/compression, bi-axial bending and warping torsion. The expression for the axial strain is expressed as

$$\varepsilon_x = \frac{du}{dx} - \frac{d^2v}{dx^2}\cdot y - \frac{d^2w}{dx^2}\cdot z - \frac{\mathrm{d}^2\varphi}{\mathrm{d}x^2}\cdot \omega(s) \tag{1}$$

where x corresponds to the direction of beam length; u, v, w is the displacement along x, y and z axis, as shown in Fig. 1(a). φ is the rotation angle of the cross section; the s coordinate coincides with the center line of the thin wall, and $\omega(s)$ is the sectorial coordinate. For an open section beam for example, the sectorial coordinate is defined as

$$\omega(s) = \int_0^s h(s)\mathrm{d}s \tag{2}$$

The integral in Eq. (3b) represents twice the area swept out by a generator rotating about the shear (rotation) center (y_{sc}, z_{sc}) of the cross-section from the point of zero warping, and $h(s)$ is the perpendicular distance from (y_{sc}, z_{sc}) to the tangent at any point s in the mid-plane of the cross-section, as illustrated in Fig. 1(b).

Depending on $\omega(s)$, the relationship between the warping displacement and rotation angle of the cross section can be established as

$$u^w = -\omega(s)\frac{\mathrm{d}\varphi}{\mathrm{d}x} \tag{3}$$

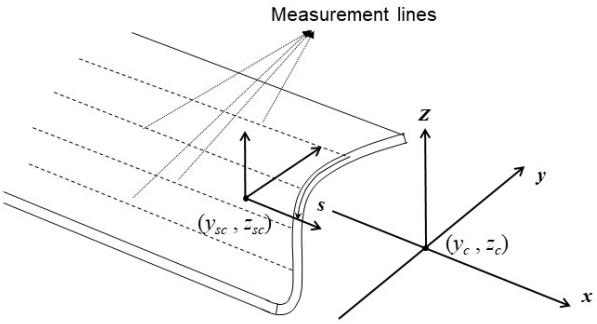

(a)

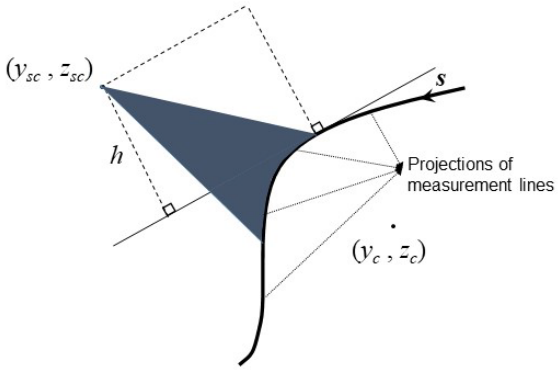

(b)

Figure 1: Diagrams of (a) a thin-walled beam structure and its (b) cross section with an arbitrary shape, with strain measurement lines installed on the beam surface along the beam length [1]

It can be seen from Eq. (1) that the derivatives of the generalized displacements, i.e., u, v, w and ϕ are all included in the equation. Thus by applying proper strain measurement strategies, the derivatives terms associated with different loading cases can be decoupled. A typical way is to assign four strain measurement line on the beam surface and along the beam axis, as shown in Fig. 1(a). So there will be four points on an arbitrarily selected cross section where axial strain values are known. The points are actually the projections of the four measurement lines onto the cross section, and thus were defined as "projections" in the following text. It can be realized that on an arbitrary cross section, a set of equations can be built according to Eq. (1), of being

$$\frac{du}{dx} - \frac{d^2v}{dx^2} \cdot y_i - \frac{d^2w}{dx^2} \cdot z_i - \frac{\mathrm{d}^2\phi}{\mathrm{d}x^2} \cdot \omega\left(s_i\right) = \varepsilon_i \quad (i=1,2,3 \text{ and } 4) \tag{4}$$

When the geometry of the section and the positions of the projections are known, the values of y_i, z_i and $\omega\left(s_i\right)$ can be readily known. So the four derivative terms, i.e., $\mathrm{d}u/\mathrm{d}x$, $\mathrm{d}^2v/\mathrm{d}x^2$, $\mathrm{d}^2w/\mathrm{d}x^2$ and $\mathrm{d}^2\phi/\mathrm{d}x^2$, are the four unknowns to be solved from the equation set. Eq. (4) corresponds to the situation where all loading cases are included. In practical application, the number of strain measurement lines can be actually arranged to be equal to the number of coupled loading case. For example, for pure torsion, Eq. (4) degenerates into

$$-\frac{\mathrm{d}^2\phi}{\mathrm{d}x^2} \cdot \omega\left(s_i\right) = \varepsilon_i \quad (i=1), \tag{5}$$

in which only a single strain measurement line is needed. In the presented study, loading cases involving bi-axial bending and torsion was studied, so the equation set can be established as

$$-\frac{d^2v}{dx^2}\cdot y_i-\frac{d^2w}{dx^2}\cdot z_i--\frac{\mathrm{d}^2\varphi}{\mathrm{d}x^2}\cdot\omega\left(s_i\right)=\varepsilon_i \quad (i=1, 2, 3) \tag{6}$$

where three lines of strain measurement are required.

2.2 Deformed Shape Reconstruction Under Individual Loading Cases

After obtaining the derivative terms of the generalized displacements, the distributions of the displacements can be further calculated along the beam axis. Assuming there are n+1 strain measurement points along each measurement line. The adjacent distance between measurement points is assumed to be uniform to be Δ. Thus n+1 sets of equations can be established corresponding to n+1 cross sections, by solving which the distributions of the derivative terms along the beam axis can be obtained. Assuming $x_{i\text{-}1}$ and x_i are the coordinate values of the adjacent measurement points, i-1 and i, along the beam axis. Within the region $x_{i-1}<x<x_i$, the distribution the derivative terms is assumed to be linear, expressed as

$$\lambda\left(x\right)=\lambda_{i-1}-\left(\lambda_{i-1}-\lambda_i\right)\frac{x-x_{i-1}}{\Delta}, \qquad x_{i-1}<x<x_i, \tag{7a}$$

In Eq. (7a), λ is defined as the generalized derivative term, which means λ can be regarded as du/dx, d^2v/dx^2, d^2w/dx^2 or $\mathrm{d}^2\phi/\mathrm{d}x^2$. The generalized displacements were then calculated based on piece-wise integration formulation relying on Eq. (7a), provided the boundary conditions of the beam are known. Specifically, the first and second-order integrations of λ at measurement point i were derived as

$$\lambda_i^{\mathrm{I}}=\frac{\Delta l}{2}\left[\lambda_0+2\sum_{j=1}^{i-1}\lambda_j+\lambda_i\right]+\lambda_0^{\mathrm{I}}, \qquad i=1, 2,..., n \tag{7b}$$

and

$$\lambda_i^{\mathrm{II}}=\frac{\Delta^2}{6}\left[\left(3i-1\right)\lambda_0+6\sum_{j=1}^{i-1}\left(i-j\right)\lambda_j+\lambda_i\right]+\Delta\lambda_0^{\mathrm{I}}+\lambda_0^{\mathrm{II}}, \qquad i=1, 2,..., n \tag{7c}$$

where λ_0^{I} and λ_0^{II} are boundary values at x_0. For a cantilever beam clamped at x_0 in particular, $\lambda_0^{\mathrm{I}}=\lambda_0^{\mathrm{II}}=0$. For beams subject to other types of boundary conditions, the forms of Eqs. (7b) and (7c) can be easily adjusted. For example, to calculate bending deflection of a simply supported beam, boundary conditions of deflections at the two ends of the beam can be used in adjusted equations. As clearly seen, the first-order integration algorithm, i.e., Eq. (7b), is used to calculate the distribution of the first-order integration of the derivative terms, that are u, dv/dx, dw/dx and $\mathrm{d}\varphi/\mathrm{d}x$, where u is the tension/compression displacements; dv/dx and dw/dx are related to the bending angles of the beam; and $\mathrm{d}\varphi/\mathrm{d}x$ is related to the warping displacement, u^w, as expressed in Eq. (3a). Furthermore, the second-order integration algorithm, i.e., Eq. (7c), can be used to calculate the distributions of v, w and φ.

The specific expressions of Eqs. (7b) and (7c) for uni-axial bending was given in Ko et al. [17], as

$$\tan\theta_i=\frac{\Delta}{2c}\left[\varepsilon_0+2\sum_{j=1}^{i-1}\varepsilon_j+\varepsilon_i\right]+\tan\theta_0, \qquad i=1, 2,..., n \tag{8a}$$

and

$$y_i=\frac{\Delta^2}{6c}\left[\left(3i-1\right)\varepsilon_0+6\sum_{j=1}^{i-1}\left(i-j\right)\varepsilon_j+\varepsilon_i\right]+\Delta\tan\theta_0+y_0, i=1, 2,..., n \tag{8b}$$

where θ and y represent bending angle and deflection, respectively.

And the specific expressions for warping torsion was developed in [1], written as

$$u_i^w(s)=\frac{\Delta\omega(s)}{2\omega(s_m)}\left[\varepsilon_0+2\sum_{j=1}^{i-1}\varepsilon_j+\varepsilon_i\right]+\frac{\omega(s)}{\omega(s_m)}u_0^w(s_m),\qquad i=1,2,...,n \tag{9a}$$

and

$$\varphi_i=-\frac{(\Delta l)^2}{6\omega(s_m)}\left[(3i-1)\varepsilon_0+6\sum_{j=1}^{i-1}(i-j)\varepsilon_j+\varepsilon_i\right]+\Delta l\frac{u_0^w(s_m)}{\omega(s_m)}+\varphi_0,\ i=1,2,...,n \tag{9b}$$

where $\omega(s_m)$ is the sectorial coordinate of the projections of measurement lines; $\omega(s)$ is the sectorial coordinate of the projections of any arbitrary line along the beam axis.

2.3 Full-Field Deformed Shape Reconstruction

Depending on Eqs. (7b)-(7c), the distributions of the generalized displacements subject to individual loading cases, i.e., *u*, *v*, *w* and ϕ, can be calculated. Next, the actually full-field deformed shapes of the thin-walled beam can be constructed, according to

$$\begin{aligned}
&u_x(x,y,z)=u(x)+z\theta_y(x)-y\theta_z(x)+u^w(x),\\
&v_y(x,y,z)=v(x)-z\varphi(x),\\
&w_z(x,y,z)=w(x)+y\varphi(x).
\end{aligned} \tag{10}$$

where $u_x(x,y,z)$, $v_x(x,y,z)$ and $w_x(x,y,z)$ are the full-field displacements of the beam under complex loading cases; β_z and β_y are the rotation angles referring to *z* and *y* axis on the cross section, respectively. The values of β_z and β_y can be calculated by using the relationships of $\tan\beta_z=\mathrm{d}v/\mathrm{d}x$ and $\tan\beta_y=\mathrm{d}w/\mathrm{d}x$, respectively.

3 Deformation Reconstruction Under Warping Torsion

Deformed shape reconstruction of an aluminum isotropic Euler-Bernoulli cantilever beam with thin-walled channel section was carried out based on finite element analysis (FEA). The beam is shown in Fig. 2(a). The length of the hat section beam is 1000 mm, and the detailed section dimension is shown in Fig. 2(b). Fig. 2(c) provides the distribution of sectorial coordinate, $\omega(s)$, along the mid-plane of the channel section. Strain measurement lines were arranged on the beam surface along the direction of beam axis. Along each measurment line, there are 101 measurement points, distributing with an uniform adjacent distance to be 10 mm. The FE model of the beam was built by using commercial FEA software (ANSYS®) using three-dimensional block elements. The values of axial strains were extracted at every measurement point from the FEA results.

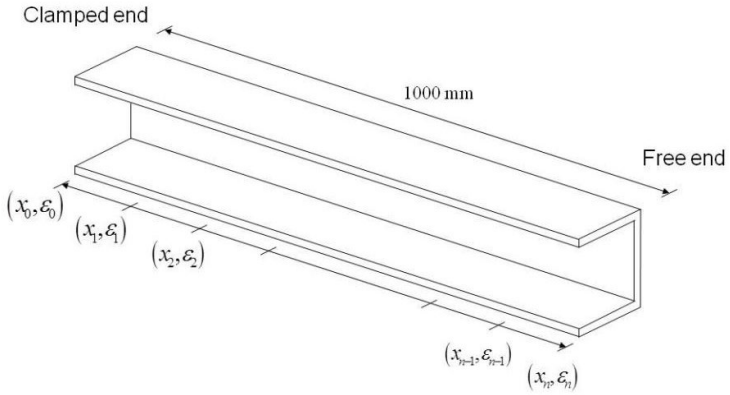

(a)

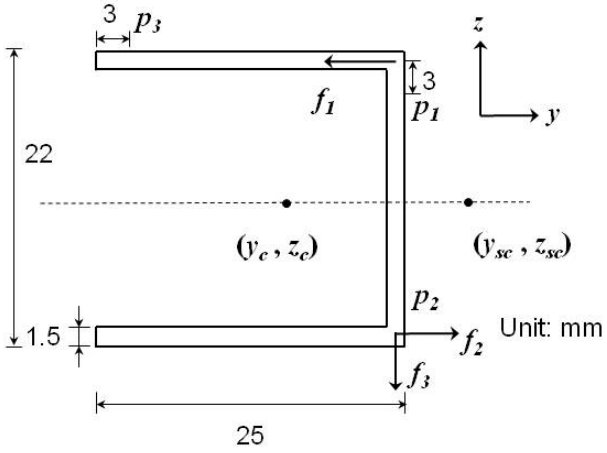

(b)

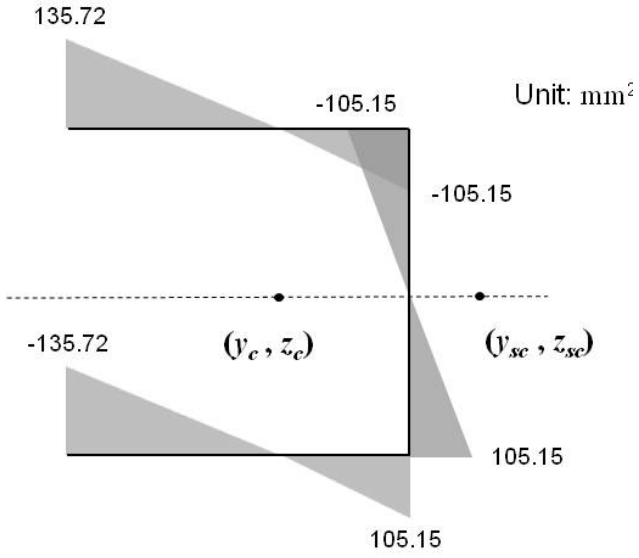

(c)

Figure 2: (a) Three-dimensional view and (b) the cross section of a thin-walled channel section beam, and (c) the distribution of the sectorial coordinate across the mid-plane of the cross section

To construct pure torsion deformation, only a single measurement line is needed as stated previously. A measurement line was arranged on the beam surface, with projections denoted as p_1 as shown in Fig. 2(b). Since warping displacements were considered with less importance in engineering applications compared to rotation angles. Only rotation angles were reconstructed and analyzed.

Direct FEA was performed under counterclockwise torques, which were applied using two concentrated forces, $\boldsymbol{f}_1$ and $\boldsymbol{f}_2$, at the free end, shown in Fig. 2(b). The forces are symmetric with the symmetrical axis of the beam section. The rotation angles of the beam were reconstructed under different torque levels of 0.22, 0.44, 0.66 and 0.88 Nm, respectively, as presented in Figs. 3(a)-3(d). The exact values of the rotation angles were calculated using the nodal displacements of the FEA results for comparison.

It is observed from Fig. 3 that significant agreement can be seen between the reconstructed and FEA results, implying a significantly high accuracy of rotation angle reconstruction. Moreover, it is apparent that the reconstruction accuracy decreases along with enlarged torsion deformation. From Figs. 3(a)-3(d), the relative reconstruction error at the free end of the beam are 0.14%, 0.58%, 1.77% and 3.39%, respectively.

The reconstruction accuracy associated with another position of the measurement line, denoted as p_3 shown in Fig. 2(b), was examined subsequently. The reconstructed and FEA-based rotation angles subject to different torque levels are shown in Figs. 4(a)-4(d). Satisfactory reconstruction accuracy can be seen. The relative reconstruction errors at the free end are 3.2%, 2.9%, 3.5% and 4.6%, respectively. By comparing Figs. 3-4, it is certain that the variation of measurement positions will influence the accuracy of deformation reconstruction. And in the presented case, reconstruction accuracy associated with position p_1 is higher than that associated with p_3.

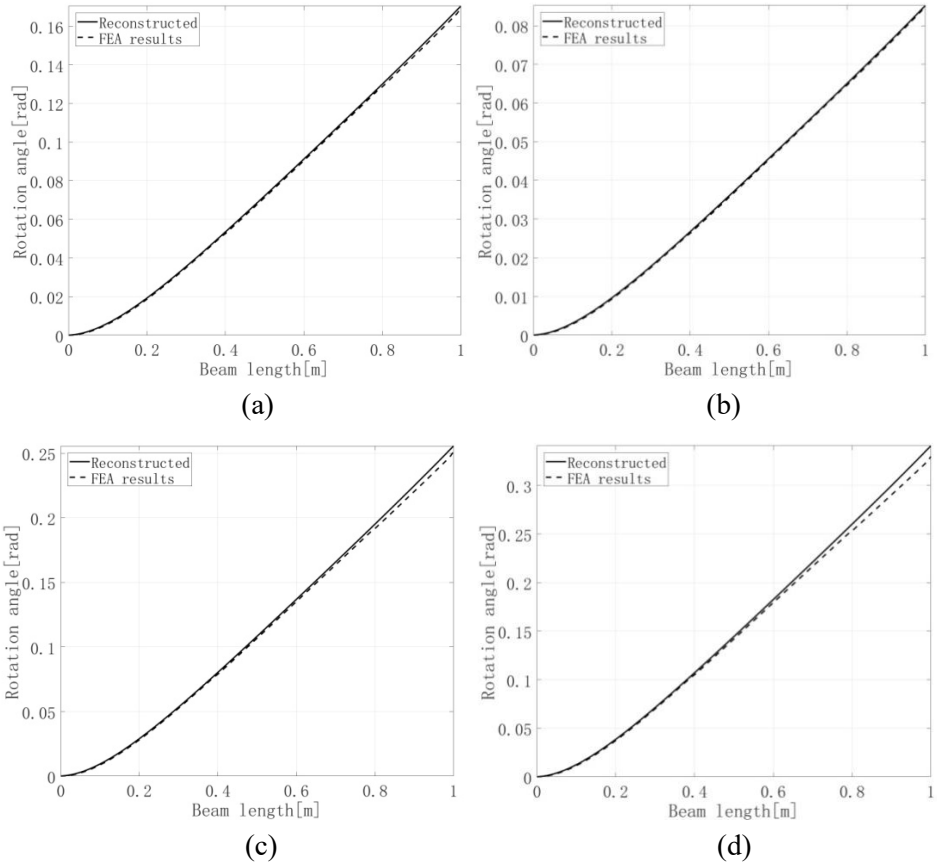

Figure 3: Reconstructed and FEA-based rotation angles subject to torque levels of (a) 0.22 (b) 0.44 (c) 0.66 and (d) 0.88 Nm. The reconstructed rotation angles were based on strain measured along p_1 shown in Fig. 2(b)

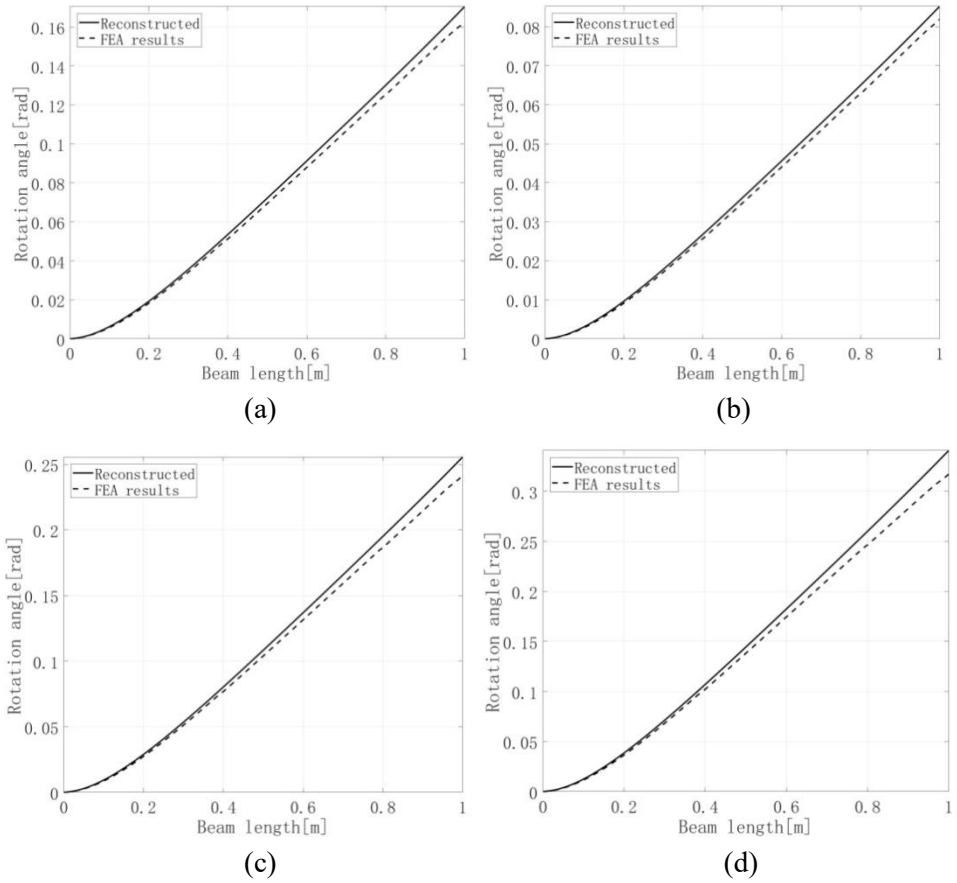

Figure 4: Reconstructed and FEA-based rotation angles subject to torque levels of (a) (b) (c) and (d). The reconstructed rotation angles were based on strain measured along p_3 shown in Fig. 2(b)

In practical measurement, the influence of measurement noise is regarded as a vital factor that may largely limit the accuracy of deformed shape reconstruction accuracy in this study. Thus measurement noise was introduced numerically into the strains extracted from the FEA to simulate actually measurement condition. The noise was introduced in terms of

$$\varepsilon_i^{noisy} = \varepsilon_i^{exact} \Delta\varepsilon \tag{11}$$

where ε_i^{noisy} and ε_i^{exact} are the noise-free strain obtained at measurement point i from simulation and its corresponding noise-polluted counterpart; $\Delta\varepsilon$ is a Gaussian random real number related to the magnitude of ε_i^{exact}. The mean of $\Delta\varepsilon$ is one, and the standard deviation of $\Delta\varepsilon$ is deemed as the level of measurement noise (referred to as noise level) in the following studies.

Figs. 5(a)-5(d) show the strain distributions along p_1 (in Fig. 2(b)) under torque of 0.88 Nm, with noise levels of being 5%, 10%, 20% and 30%, respectively. The exact strain distributions from the FEA were also plotted for comparison. It is observed that the strain signals were increasingly disturbed along with increased noise levels. And under noise level of 20% and 30%, the noise influence on the exact strains was observed to be highly severe.

Based on the noise contaminated strains as shown in Figs. 5(a)-5(d), the rotation angles of the beam were reconstructed and compared with the FEM-based results. The reconstructed and FEM-based rotation angles are shown in Figs. 6(a)-6(d), subject to noise level of 5%, 10%, 20% and 30%, respectively. It is impressive to observe that despite of severe noise interference in the strain distribution, up to noise level of 30%, as shown in Fig. 5. Significantly accuracy of reconstruction can be well preserved. In Figs. 6(a)-

6(d), the averaged relative reconstruction errors at the free end of the beam are 4.0%, 4.8%, 5.4% and 7.4%, respectively. It should be noted that for all subsequent analysis related to noise influence, the relative reconstruction errors at the free end were evaluated by perform 50 times of average of the absolute values of the relative errors of individual simulations. The averaged results can be deemed as the standard deviations of the relative reconstruction errors.

A detailed presentation of the averaged relative reconstruction errors at the free end of the beam, subject to different torques and noise levels, is given in Tab. 1. It can be clearly seen from the table that the reconstruction error increase with the increases of both torque and noise levels. The maxim error reaches 7.44%, corresponding to torque of 0.88 Nm and noise level of 30%.

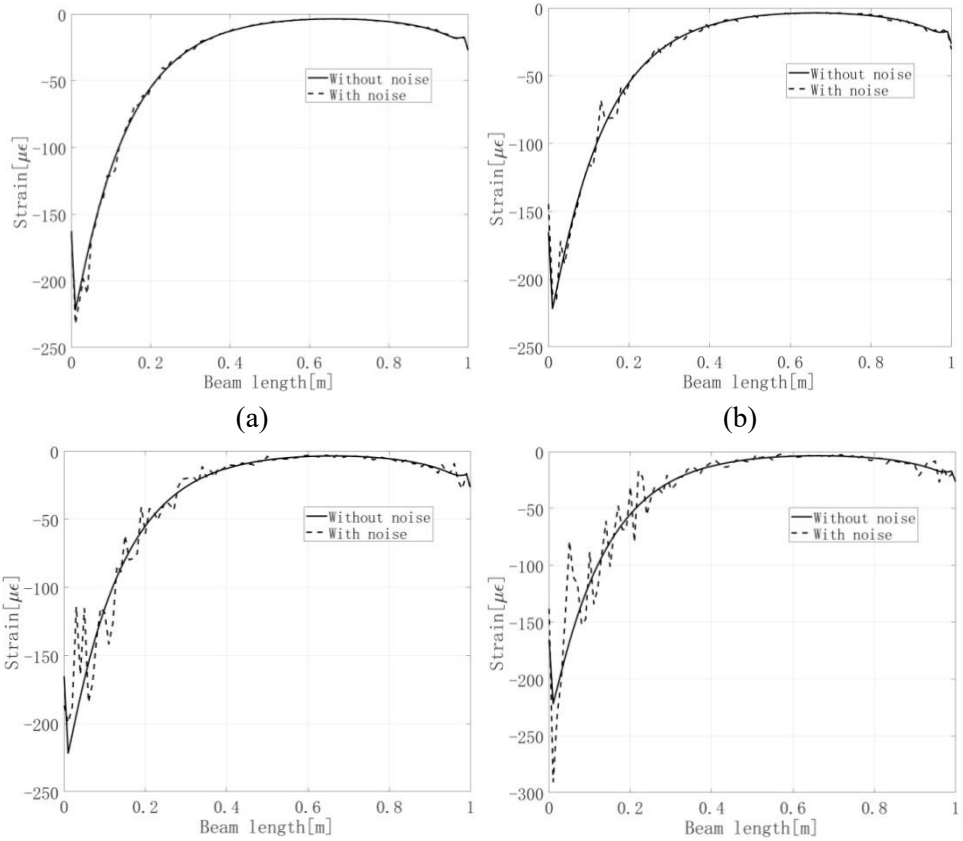

Figure 5: Distributions of strains with and without noise influence subject to torque of 0.88Nm. The noise levels contained in the strain signals are (a) 5%, (b) 10%, (c) 20% and (d) 30%, respectively

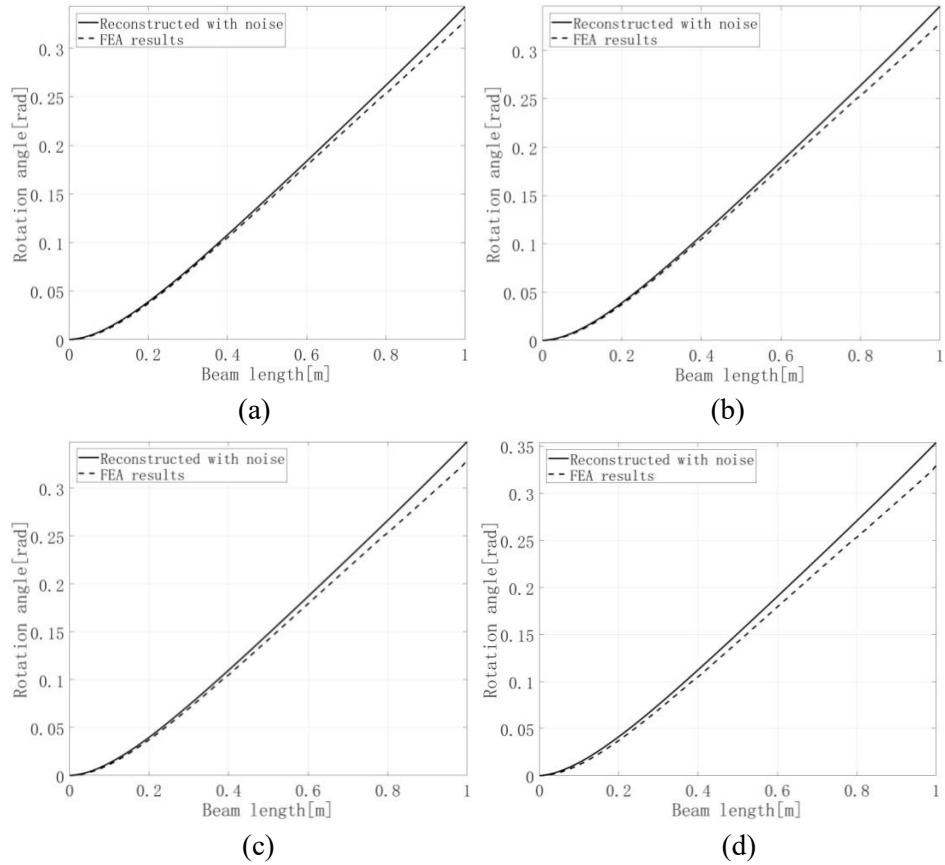

Figure 6: Reconstructed and FEA-based rotation angles subject to torque of 0.88Nm, and noise levels of (a) 5%, (b) 10%, (c) 20% and (d) 30%, respectively

Table 1: Averaged relative reconstruction errors in rotation angles at the free end of the beam subject to different levels of torques and noise levels

Noise level	Torque [Nm]	Averaged relative reconstruction error [%]
Without noise	0.22	0.14
	0.44	0.58
	0.66	1.77
	0.88	3.39
5%	0.22	0.52
	0.44	1.11
	0.66	1.81
	0.88	3.99
10%	0.22	1.11
	0.44	1.92
	0.66	2.89
	0.88	4.75

20%	0.22	2.25
	0.44	2.89
	0.66	3.49
	0.88	5.35
30%	0.22	4.36
	0.44	3.87
	0.66	4.82
	0.88	7.44

4 Deformation Reconstruction Under the Coupling Between Bi-Axial Bending and Warping Torsion

Deformation coupling between bi-axial bending and warping torsion was applied by adding two concentrated forces, i.e., f_1 and f_3, simultaneously at the free end of the channel section beam. The location of the concentrated forces is presented in Fig. 2(b). It should be noted that because of the asymmetric geometric property of the channel cross section, a single concentrated force alone, e.g., f_3, is sufficient to induce deformation coupling between bi-axial bending and torsion. However, to prevent too small deformation along y axis, f_2 was added in the horizontal direction. The magnitudes of f_1 and f_3, were settled to be the same. Four levels of loadings were applied in the following cases, i.e., $f_1 = f_3 = 20$, 40, 60 and 80 N. To evaluate the accuracy of the reconstruction of deformed shapes, the displacements of the beam in y and z direction and the rotation angles were calculated based on the nodal displacements of the FEA results for comparison. Strains along three measurement lines, i.e., p_1, p_2 and p_3 in Fig. 2(b), were used to reconstruct the deformed shapes. The reconstructed displacement distributions along y axis, $v(x)$, across the beam length are shown in Figs. 7(a)-7(d). It can be seen that for bending deformation reconstruction, the accuracy of deformed shape reconstruction is relatively stable subject to the given four loading cases. The relative reconstruction errors at the free end are around 1.8%. The distributions of displacement along z axis, $w(x)$, across the beam length under the four loading levels are presented in Fig. 8(a)-8(d). As predicted, the accuracy of reconstruction presented in the four figures are basically the same, with relative errors of being around 2.6%. The reconstructed and FEA-based rotation angles are presented in Figs. 9(a)-9(d). The relative errors at the free end are around 1%, 0.6%, 3% and 8%, respectively. The reconstructed and the FEA-based curve intersected during the increase of the loading level, as shown from Figs. 9(a)-9(c). Thus the relative error in Fig. 9(b) is even smaller than in (a). In general, the reconstruction accuracy decreases along with enlarged loading levels. The observation is the similar with that in pure torsion case in Section 3.

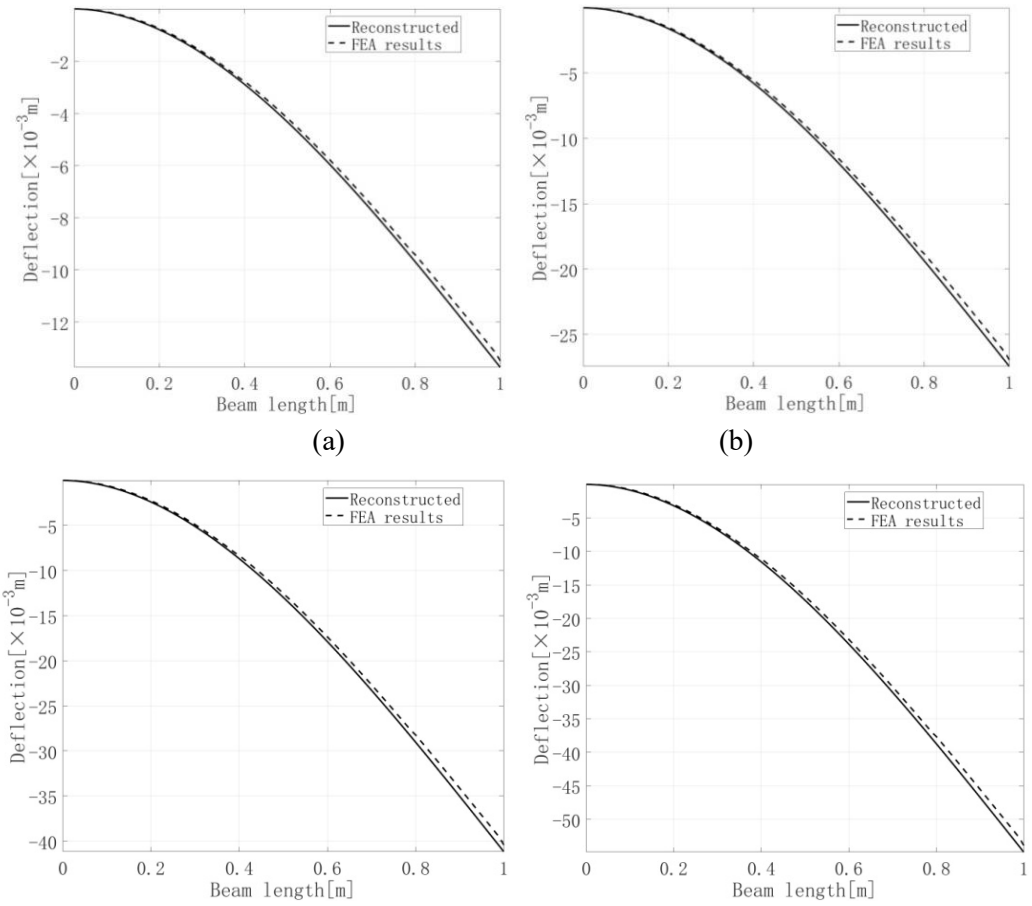

Figure 7: Reconstructed and FEA-based $v(x)$ subject to $f_1 = f_3 =$ (a) 20, (b) 40, (c) 60 and (d) 80 N, respectively

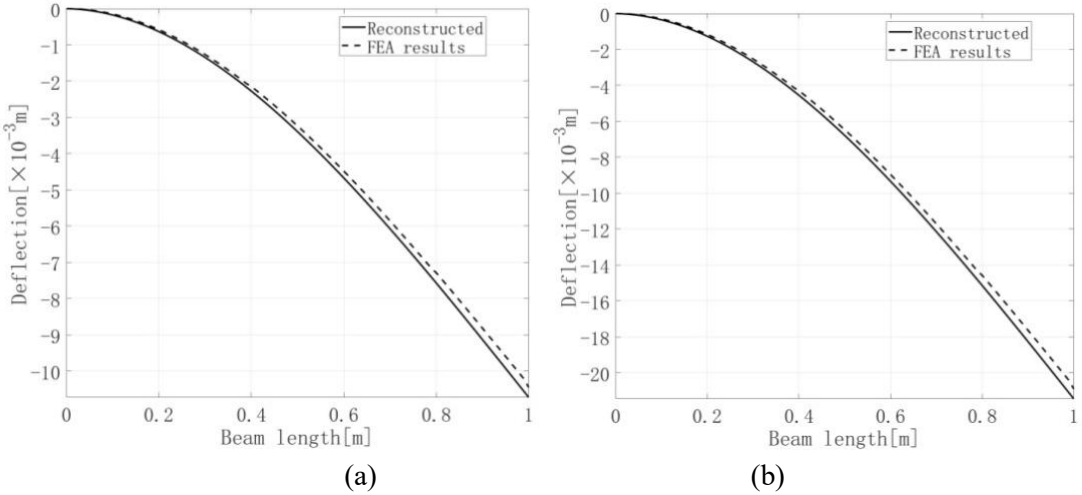

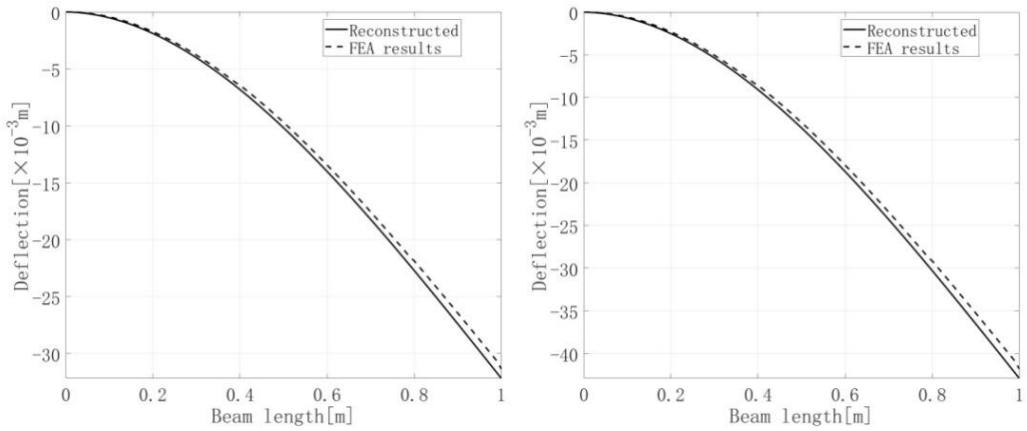

Figure 8: Reconstructed and FEA-based $w(x)$ subject to $f_1 = f_3 =$ (a) 20, (b) 40, (c) 60 and (d) 80 N, respectively

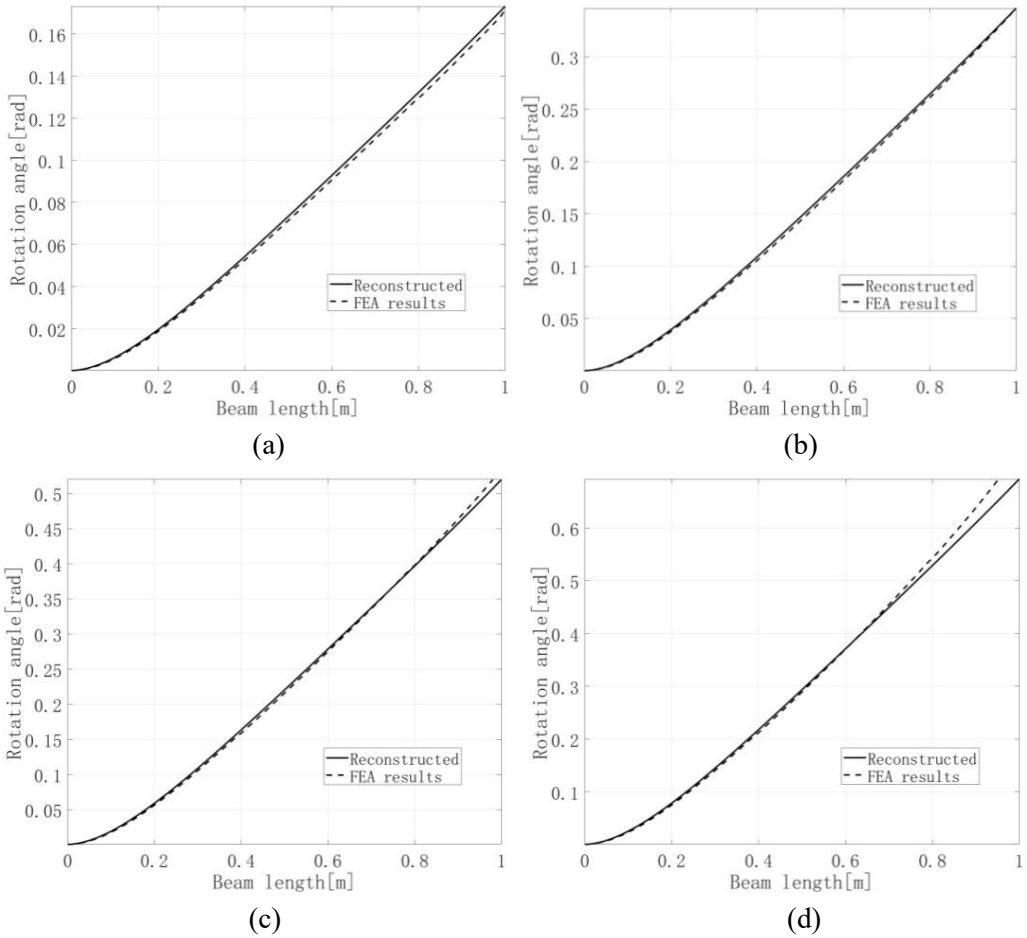

Figure 9: Reconstructed and FEA-based rotation angles subject to $f_1 = f_3 =$ (a) 20, (b) 40, (c) 60 and (d) 80 N, respectively

The influence of measurement noise was then considered for the reconstruction of deformed shapes. Measurement noise with different levels were added in the strains along all the three measurement lines, i.e., p_1, p_2 and p_3, according to the algorithm shown in Eq. (10). Similar with the pure torsion case, the noise levels were set to be 5%, 10%, 20% and 30%. Figs. 10(a)-10(d) show the reconstructed $v(x)$ along

the beam length under the four noise levels. It can be seen that the accuracy of reconstruction can be well preserved under quite large noise levels. Under noise level of 30%, the accuracy decreases largely. The averaged relative reconstruction errors at the free end in Figs. 10(a)-10(d) are 2.4%, 2.9%, 4.4% and 4.8%, respectively. Figs. 11(a)-11(d) present the reconstructed $w(x)$. The same trend of reconstruction accuracy along with increased noise levels can be observed. The averaged relative reconstruction errors at the free end in Figs. 11(a)-11(d) are 3.3%, 4.0%, 5.7% and 7.2.%, respectively. The reconstructed and FEA-based rotation angles under different noise levels are presented in Figs. 12(a)-12(d). It is seen that the noise immunity of torsion deformation is still acceptable. The averaged relative reconstruction errors of rotation angels at the free end are 4.9%, 5.7%, 8.5% and 9.7%, respectively, where Fig. 12(d) is considered to be largely influenced by measurement noise.

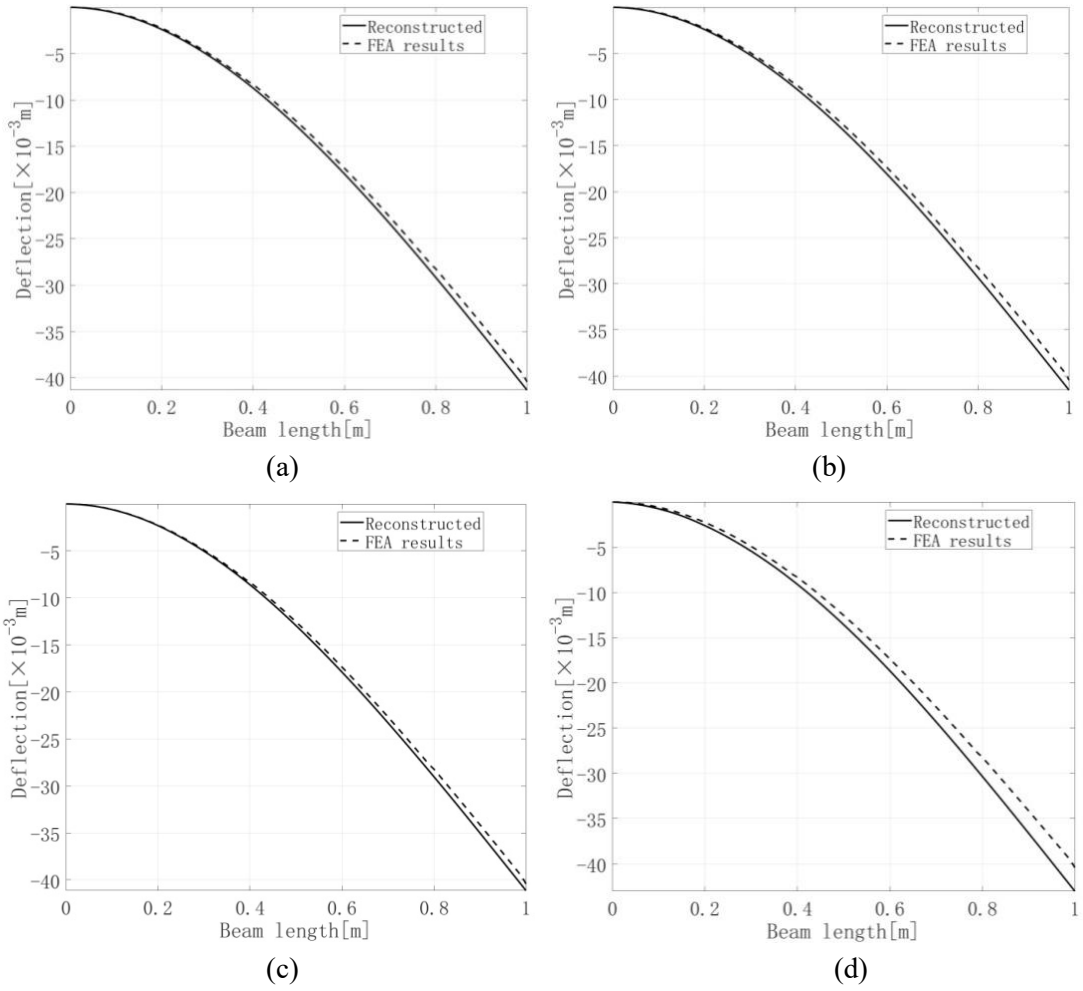

Figure 10: Reconstructed and FEA-based $v(x)$ subject to $f_1 = f_3 = 60$ N, and noise levels of (a) 5%, (b) 10%, (c) 20% and (d) 30%, respectively

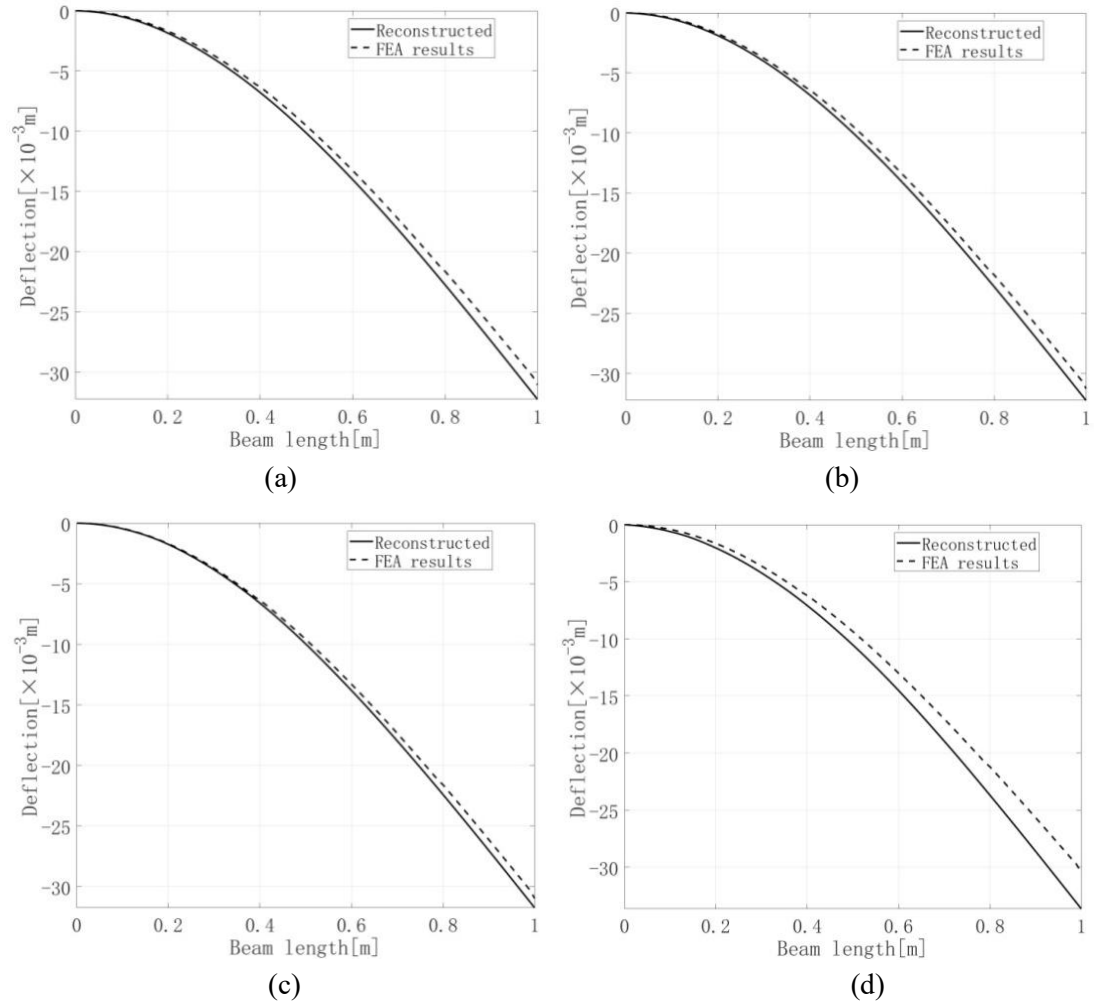

Figure 11: Reconstructed and FEA-based $w(x)$ subject to $f_1 = f_3 = 60$ N, and noise levels of (a) 5%, (b) 10%, (c) 20% and (d) 30%, respectively

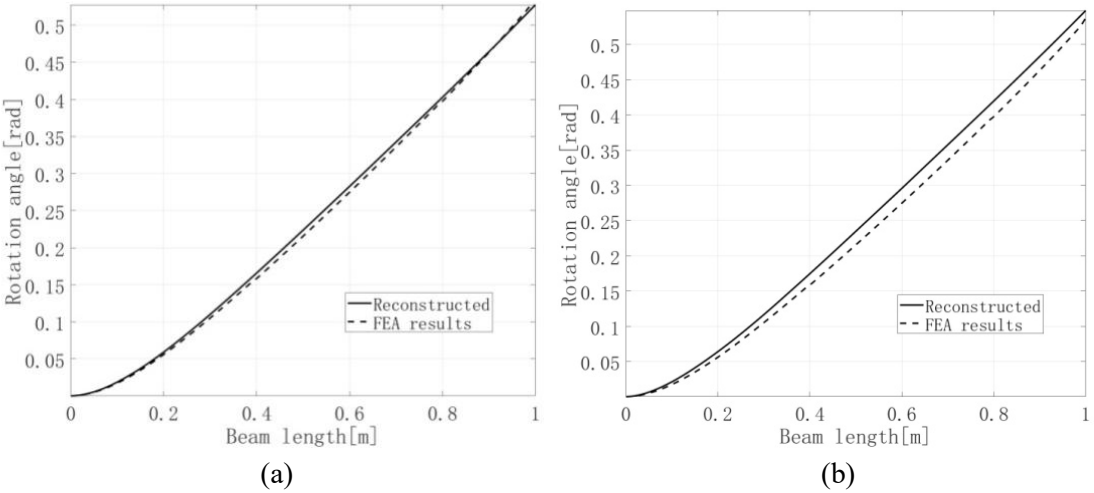

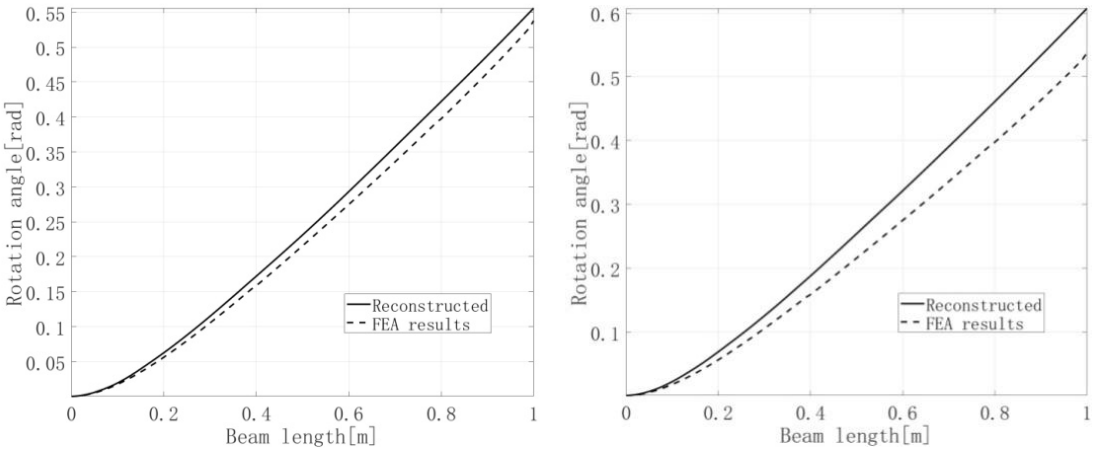

Figure 12: Reconstructed and FEA-based rotation angles subject to $f_1 = f_3 = 60$ N, and noise levels of (a) 5%, (b) 10%, (c) 20% and (d) 30%, respectively

More detailed presentation of the reconstruction accuracy under different loading levels and noise levels are given in Tabs. 2-4. It can be seen that most of the averaged relative reconstruction errors are kept within an acceptable range (e.g., within 10%). A general trend is demonstrated with certainty that the reconstruction accuracy decreases with enlarged loading levels and increased degree of noise interference. The noise immunity of rotation angle reconstruction is inferior to that of bending deflection reconstruction. The largest relative error of rotation angle reconstruction can be found to be 16.52%, associated with loading level of $f_1 = f_3 = 80$ N and noise level of 30%.

Table 2: Averaged relative reconstruction errors in $v(x)$ at the free end of the beam subject to different magnitudes of concentrated forces and noise levels

Noise level	Force magnitude [N]	Averaged relative reconstruction error [%]
Without noise	20	1.84
	40	1.84
	60	1.84
	80	1.84
5%	20	2.27
	40	2.39
	60	2.35
	80	2.34
10%	20	3.01
	40	2.82
	60	2.86
	80	2.97
20%	20	4.20
	40	3.70
	60	4.35
	80	3.32

30%	20	4.87
	40	5.65
	60	4.82
	80	4.90

Table 3: Averaged relative reconstruction errors in $w(x)$ at the free end of the beam subject to different magnitudes of concentrated forces and noise levels

Noise level	Force magnitude [N]	Averaged relative reconstruction error [%]
Without noise	20	2.63
	40	2.63
	60	2.63
	80	2.63
5%	20	3.24
	40	3.35
	60	3.26
	80	3.35
10%	20	4.15
	40	3.98
	60	4.02
	80	4.08
20%	20	6.03
	40	5.00
	60	5.73
	80	4.61
30%	20	7.17
	40	7.51
	60	7.17
	80	6.89

Table 4: Averaged relative reconstruction errors in rotation angles at the free end of the beam subject to different magnitudes of concentrated forces and noise levels

Noise level	Force magnitude [N]	Averaged relative reconstruction error [%]
Without noise	20	0.95
	40	0.59
	60	3.37
	80	7.84
5%	20	2.33
	40	1.78
	60	4.93
	80	9.11

10%	20	4.47
	40	3.23
	60	5.72
	80	10.28
20%	20	6.00
	40	5.93
	60	8.52
	80	12.13
30%	20	9.52
	40	9.01
	60	9.74
	80	16.52

5 Conclusion

In this study, the effectiveness of a recently proposed deformation reconstruction method was demonstrated using a channel section thin-walled beam under the coupling among complex loading cases, i.e., the combination between bi-axial bending and warping torsion. Using the developed set of equations for deformation decoupling, the displacements along the *y* axis, the *z* axis and the rotation angles were decoupled. And the distributions of the deformed shapes along the beam length were then constructed. The effectiveness and accuracy of the method was examined relying on analysis results of finite element analysis (FEA). In the analysis, the influence of the positions of the measurement of surface strain distributions on the reconstruction accuracy was discussed. Moreover, different levels of measurement noise were added to the axial strain values based on numerical method, and the noise resistance ability of the deformation reconstruction method was investigated systematically. According to the FEA results, the effectiveness and precision of the method in complex deformation decoupling and reconstruction as was demonstrated. It is observed that under the given loading situations, reconstruction accuracy of rotation angles is more vulnerable to enlarged loading levels than that of bending deformations. On the other hand, the reconstruction accuracy decreases with increased noise levels. The noise immunity of rotation angle reconstruction is inferior to that of bending deflection reconstruction. To conclude, the noise immunity of the deformed shape reconstruction method for complex loading involving coupling between bi-axial bending and warping torsion is proven to be strong up to considerably large noise level of being 30%.

Acknowledgement: This research was supported by the National Science Foundation of China (No. 11602048 and No. 51805068).

References

1. Xu, H., Zhou, Q., Lu, R., Gao, C., Wu, Z. (2019). Reconstructing full-field complex deformations of thin-walled beam structures based on in-situ strain measurement (Submitted to Smart Matierials and Structures).
2. Su, Z., Ye, L., Lu, Y. (2006). Guided Lamb waves for identification of damage in composite structures: a review. *Journal of Sound & Vibration, 295(3),* 753-780.
3. Zhou, K., Xu, X., Zhao, Z., Yang, Z., Zhou, Z. et al. (2018). Excitation of plane lamb wave in plate like structures under applied surface loading. *Smart Material Structures, 27(2)*.
4. Cai, J., Yuan, S., Qing, X., Chang, F., Shi, L. et al. (2015). Linearly dispersive signal construction of Lamb waves with measured relative wavenumber curves. *Sensors & Actuators A: Physical, 221,* 41-52.
5. Koduru, J. P., Momeni, S., Rose, J. L. (2013). Phased annular array transducers for omnidirectional guided wave mode control in isotropic plate like structures. *Smart Material Structures, 22(*12).
6. Farrar, C. R., Doebling, S. W., Nix, D. A. (2001). Vibration-based structural damage identification.

Philosophical Transactions of the Royal Society of London. Series A: Mathematical, Physical and Engineering Sciences, 359(1778), 131-149.

7. Fan, W., Qiao, P. (2011). Vibration-based damage identificationmethods: a review and comparative study. *Structural health monitoring, 10(1),* 83-111.
8. Cao, M. S., Ostachowicz, W., Bai, R. B., Radzienski, M. (2013). Fractalmechanism for characterizing singularity of mode shape for damage detection. *Applied Physics Letters, 103(22)*.
9. Xu, H., Cheng, L., Su, Z., Guyader, J. L. (2011). Identification of structural damage based on locally perturbed dynamic equilibrium with an application to beam component. *Journal of Sound and Vibration, 330(*24*),* 5963-5981.
10. Xu, H., Su, Z., Cheng, L., Guyader, J. L. (2017). On a hybrid use of structural vibration signatures for damage identification: A virtual vibration deflection (VVD) method. *Journal of Vibration and Control, 23(4),* 615-631.
11. Nicolas, M. J., Sullivan, R. W., Richards, W. L. (2016). Large scale applications using FBG sensors: determination of in-flight loads and shape of a composite aircraft wing. *Aerospace, 3(3),* 18.
12. Lokos, W. A. (1990). Predicted and measured in-flight wing deformations of a forward-swept-wing aircraft. *NASA TM 4245*.
13. Meng, X., Roberts, G. W., Dodson, A. H., Cosser, E., Barnes, J. et al. (2004). Impact of GPS satellite and pseudolite geometry on structural deformation monitoring: analytical and empirical studeis. *Journal of Geodesy, 77(12),* 809-822.
14. Roberts, G. W., Cosser, E., Meng, X., Dodson A. (2004). High frequency deflection monitoring of bridges by GPS. *Journal of Global Positioning Systems, 3(1-2),* 226-231.
15. Psimoulis, P. A., Stiros, S. C. (2007). Measurement of deflection and of oscillation frequencies of engineering structures using Robotic Theodolites (RTS). *Engineering Structures, 29(12),* 3312-3324.
16. Shi, C., Luo, X., Qi, P., Li T., Song S. et al. (2017). Shage sensing techniques for continuum robots in minimally invasive surgery: a survey. *IEEE Transactions on Biomedical Engineering, 64(8),* 1665-1678.
17. Ko, W. L., Richards, W. L., Tran, V. T. (2007). *Displacement theories for in-flight deformed shape predictions of aerospace structures*. NASA Dryden Flight Research Center, Rept. 214612, Hampton, Virginia.
18. Jutte, C. V., Ko, W. L. Stephens, C. A. (2011). *Deformed shape calculation of a full-scale wing using fiber optic strain data from a ground loads test*. NASA Langley Research Center, Rept. TP-215975, Hampton, Virginia.
19. Ko, W. L., Fleischer, V. T. (2013). *Large-deformation displacement transferfunctions for shape predictions of highly flexible slender aerospace structures*. NASA Langley Research Center, Rept. TP-216550, Edwards, California.
20. Foss, G., Haugse, E. (1995). Using modal test results to develop strain to displacement transformations. *Proceedings of 13th International Conference on Modal Analysis, Nashvile Tennessee,* 112-128.
21. Bogert, P., Haugse, E.; Gehrki, R. (2003). Structural shape indentification from experimental strains using a modal transformation technique. *44th AIAA/ASME/ASCE/AHS/ASC Structures, Structural Dynamic, and Materials Conference,* 1-18.
22. Tessler, A., Spangler, J. L. (2004). Inverse FEM for full-field reconstruction of elastic deformations in shear deformable plates and shells. *Proceedings of the 2nd European Workshop on Structural Health Monitoring, Munich.*
23. Tessler, A., Spangler, J. L., Mattone, M., Gherlone, M., Di Sciuva, M. (2011). Real-time characterization of aerospace structures using onboard strain measurement technologies and inverse Finite element method. *Proceedings of the 8th International Workshop on Structural Health Monitoring. Stanford.*
24. Miller, E. J., Manalo, R., Tessler, A. (2016). Full-field reconstruction of structural deformations and loads from measured strain data on a wing test article using the inverse finite element method. *NASA/TM-2016-219407.*
25. Vazquez, S. L., Tessler, A., Quach, C. C., Cooper, E. G., Parks, J. et al. (2005). Structural health monitoring using high-density fiber optic strain sensor and inverse finite element methods. *NASA/TM-2005-213761.*
26. Gherlone, M., Cerracchio, P., Mattone, M., Sciuva, M., Tessler, A. (2014). An inverse finite element method for beam shape sensing: theoretical framwork and experimental validation. *Smart Materials and Structures, 23(4)*.
27. Loughlan, J., Ata, M. (1995). The restrained torsional response of open section carbon fiber composite beams. *Composite Structures, 32(1-4),* 13-31.

28. Loughlan, J., Ata, M. (1998). The analysis of carbon fibre composite box beams subjected to torsion with varaiable twist. *Computer Methods in Applied Mechanics and Engineering, 152(3-4),* 373-391.